

# **POWER SCALING FIBER AMPLIFIERS USING VERY-LARGE-MODE-AREA FIBERS**

**John Marciante**

**23 February 2016**

**Final Report**

**APPROVED FOR PUBLIC RELEASE. DISTRIBUTION IS UNLIMITED.**



**AIR FORCE RESEARCH LABORATORY  
Directed Energy Directorate  
3550 Aberdeen Ave SE  
AIR FORCE MATERIEL COMMAND  
KIRTLAND AIR FORCE BASE, NM 87117-5776**

## NOTICE AND SIGNATURE PAGE

Using Government drawings, specifications, or other data included in this document for any purpose other than Government procurement does not in any way obligate the U.S. Government. The fact that the Government formulated or supplied the drawings, specifications, or other data does not license the holder or any other person or corporation; or convey any rights or permission to manufacture, use, or sell any patented invention that may relate to them.

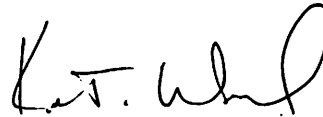
Qualified requestors may obtain copies of this report from the Defense Technical Information Center (DTIC) (<http://www.dtic.mil>).

AFRL-RD-PS-TR-2016-0009 HAS BEEN REVIEWED AND IS APPROVED FOR PUBLICATION IN ACCORDANCE WITH ASSIGNED DISTRIBUTION STATEMENT.



---

NADER NADERI, DR-II, DAF  
Work Unit Manager



---

KENTON T. WOOD, DR-IV, DAF  
Chief, Laser Division

This report is published in the interest of scientific and technical information exchange, and its publication does not constitute the Government's approval or disapproval of its ideas or findings.

<b>REPORT DOCUMENTATION PAGE</b>			<i>Form Approved</i> <i>OMB No. 0704-0188</i>	
Public reporting burden for this collection of information is estimated to average 1 hour per response, including the time for reviewing instructions, searching existing data sources, gathering and maintaining the data needed, and completing and reviewing this collection of information. Send comments regarding this burden estimate or any other aspect of this collection of information, including suggestions for reducing this burden to Department of Defense, Washington Headquarters Services, Directorate for Information Operations and Reports (0704-0188), 1215 Jefferson Davis Highway, Suite 1204, Arlington, VA 22202-4302. Respondents should be aware that notwithstanding any other provision of law, no person shall be subject to any penalty for failing to comply with a collection of information if it does not display a currently valid OMB control number. <b>PLEASE DO NOT RETURN YOUR FORM TO THE ABOVE ADDRESS.</b>				
<b>1. REPORT DATE (DD-MM-YYYY)</b> 02-23-2016		<b>2. REPORT TYPE</b> Final Report		<b>3. DATES COVERED (From - To)</b> 24 July 2014- 23 February 2016
<b>4. TITLE AND SUBTITLE</b>  Power Scaling Fiber Amplifiers Using Very-Large-Mode-Area Fibers			<b>5a. CONTRACT NUMBER</b> FA9451-14-1-0253	
			<b>5b. GRANT NUMBER</b>	
			<b>5c. PROGRAM ELEMENT NUMBER</b>	
<b>6. AUTHOR(S)</b>  John R. Marciante			<b>5d. PROJECT NUMBER</b>	
			<b>5e. TASK NUMBER</b>	
			<b>5f. WORK UNIT NUMBER</b> D075	
<b>7. PERFORMING ORGANIZATION NAME(S) AND ADDRESS(ES)</b>  University of Rochester, Institute of Optics 275 Hutchinson Road Rochester, NY 14627			<b>8. PERFORMING ORGANIZATION REPORT NUMBER</b>	
<b>9. SPONSORING / MONITORING AGENCY NAME(S) AND ADDRESS(ES)</b> Air Force Research Laboratory 3550 Aberdeen Ave SE Kirtland AFB. NM 87117-5776			<b>10. SPONSOR/MONITOR'S ACRONYM(S)</b> AFRL/RDLT	
			<b>11. SPONSOR/MONITOR'S REPORT NUMBER(S)</b> AFRL-RD-PS-TR-2016-0009	
<b>12. DISTRIBUTION / AVAILABILITY STATEMENT</b>  Approved for public release. Distribution is unlimited.				
<b>13. SUPPLEMENTARY NOTES</b> The views and conclusions contained in this document are those of the authors and should not be interpreted as representing the official policies, either express or implied, of the Air Force Research Laboratory or the U. S. Government. OPS-16-11957; 19 July 2016. Government Purpose Rights.				
<b>14. ABSTRACT</b> DEW-class fiber lasers are limited to below 1kW due to limited mode size and thermal issues, particularly thermal mode instability (TMI). Two comprehensive models were developed for scaling the mode area of fiber amplifiers while inclusively addressing all relevant spatial and dynamic effects. The beam propagation model was found to be too computationally intensive for design purposes. A rate-equation/kinetics model was developed and validated for accurately modeling very-large-mode-area fiber amplifiers while simultaneously including thermal lensing and TMI. This model was applied to investigate scaling to an effective 50µm core diameter. Mode-area scaling using conventional large-mode-area fibers was found to be simply not possible since the TMI threshold decreases with increased core area. Modifications in pump geometry were found to provide a modest benefit, particularly when flattening out the temperature profile along the fiber. Confined gain was studied and found to provide exceptional resilience to TMI (at least 2x increase in TMI threshold), as was originally proposed. Two new promising fiber types were developed, and both were found to exhibit features with modeled and expected resilience to TMI.				
<b>15. SUBJECT TERMS</b> Fiber amplifier, high power laser, thermal mode instability, large-mode-area fiber, ytterbium-doped fiber amplifiers, fiber laser				
<b>16. SECURITY CLASSIFICATION OF:</b>			<b>17. LIMITATION OF ABSTRACT</b>  SAR	<b>18. NUMBER OF PAGES</b>  33
<b>a. REPORT</b> Unclassified	<b>b. ABSTRACT</b> Unclassified	<b>c. THIS PAGE</b> Unclassified		
			<b>19b. TELEPHONE NUMBER (include area code)</b> 505-853-3612	

## Table of Contents

1. Introduction.....	1
2. Methods, Assumptions, and Procedures .....	1
3. Beam Propagation Model Development.....	3
3.1 Full BPM Model .....	3
3.2 Reduced BPM Model.....	4
3.3 Final BPM Model Assessment.....	5
4. Rate-Equation Model Development .....	5
4.1 Basic REM Model Definition and Validation .....	6
4.2 Modification to the REM Model.....	10
5. Core Scaling with Conventional Step-Index Fibers.....	13
5.1 Core-Diameter Scaling.....	13
5.2 Pumping Considerations .....	14
6. Novel VLMA Fiber Designs.....	17
6.1 Confined-Gain Fiber .....	18
6.2 Cladded Linear Index Graded (CLING) Fiber.....	20
6.3 Trefoil Fiber .....	22
7. Summary and Conclusions .....	24
8. List of Symbols, Abbreviations, and Acronyms.....	25
9. References.....	25

## List of Figures

1. LP <sub>01</sub> and LP <sub>11</sub> power evolution along the fiber amplifier length at various steps in time.....	8
2. LP <sub>01</sub> and LP <sub>11</sub> power at the amplifier output as a function of time over a 35-ms time span.....	9
3. Threshold pump power for the onset of thermally induced mode instability as a function of seed power.....	10
4. LP <sub>01</sub> and LP <sub>11</sub> mode lineouts for 0.06 NA fiber cores with diameter of 25 μm and 50 μm.....	11
5. Effective index difference between LP <sub>01</sub> and LP <sub>11</sub> modes for 0.06 NA fiber cores with diameter of 25 μm and 50 μm.....	12
6. Temperature variation above the local temperature 7 μm off the center of the fiber axis.....	13
7. TMI threshold for forward pumped LMA fiber as a function of core diameter.....	14
8. Thermal distribution along 25μm LMA fiber for forward, backward, and bi-directional pumping.....	15
9. LP <sub>01</sub> mode power distribution along 25μm LMA fiber for forward, backward, and bi-directional pumping, at their respective TMI thresholds.....	16
10. TMI threshold for forward, backward, and bi-directional pumping as a function of core diameter.....	16
11. Conventional gain fibers provide gain to HOMs especially when the gain is saturated.....	19
12. TMI threshold for confined-gain fiber compared to conventional LMA fiber.....	20
13. Comparison of modes between step-index and graded-index fibers.....	21
14. Modes of a LING fiber compared to modes of a conventional 50μm step-index fiber of the same average NA.....	21
15. TMI threshold for CLING fiber compared to conventional (step-index) LMA fiber.....	22
16. Lowest-order modes of a Trefoil fiber.....	23
17. TMI threshold for Trefoil fiber compared to conventional (step-index) LMA fiber.....	23
18. TMI threshold results summary for all conditions and fiber types.....	24

## 1. Introduction

Although high-power fiber amplifiers are commercially available at the 10kW level, their use in directed-energy weapon (DEW) systems require narrow linewidth, which to date has restricted their output power to below 1kW (without the use of line-broadening mechanisms) due to their limited mode size and thermal issues. Increasing the core diameter of large-mode area (LMA) fibers beyond the commercially accepted 20-25  $\mu\text{m}$  allows this limitation to be breached both by using a larger mode diameter and longer fibers for reduced thermal load. Although such very-large-mode-area (VLMA) fibers can therefore allow the reduction of nonlinear effects, their utility has to date *not* provided significant scaling due to (a) insufficient mode filtering, and (b) unacceptable mode-area reduction due to packaging, i.e. bend-induced mode deformation [1,2].

Even more critical to the degraded performance is the fiber's response to thermal effects. First, the thermal gradient caused by pump absorption leads to a thermal lens that inevitably results in spatial compression of the fundamental optical mode in the fiber [3]. Second, the dynamics of heat flow across the fiber cross-section leads to coupling of power out of the fundamental mode into higher order modes (HOMs), resulting in significant dynamic degradation of beam quality at the output of the fiber [4].

To date, comprehensive modeling of large-mode-area fibers has not yet been addressed due to the complexity of the problem. While it can be envisioned that such a comprehensive model can be computationally intensive, the core challenges lie with the simultaneous inclusion of the relevant physical mechanisms at play in the fiber amplifier: multiple mode beam propagation in the fiber, spatially resolved gain saturation, a self-consistent 3D thermal profile along the cross section and length of the fiber, and the dynamic effects of mode instabilities resulting from the interplay between all of these effects.

The goal of this program is (a) to develop a comprehensive model for scaling the mode area of fiber amplifiers while inclusively addressing all of the relevant spatial and dynamic effects, and (b) to apply the model to investigate VLMA fiber amplifiers scaling to an effective 50 $\mu\text{m}$  core diameter. The model must produce results with sufficient transparency to accurately assess the feasibility of the use of VLMA fibers for high-power fiber amplifier systems.

## 2. Methods, Assumptions, and Procedures

Two models were specifically addressed in this program: a modally resolved model and a wave propagation model. The basic modally resolved model separates the power evolution of a given mode from its spatial field distribution [5]. Spatially dependent gain saturation is carried through the population inversion, which is completely spatially resolved. Such a model had already been applied to assess beam quality in VLMA fibers [6], but required substantial development for use in this program, including: time-dependence, self-consistent heat generation, and a (perturbative) mode-coupling mechanism via the thermally generated profile. Although such a model may be lacking if all of the pertinent physics are not included, the advantages of this modally resolved model are that the physics is relatively transparent and the problem can in principle be analyzed over a very wide parameter space. More details on this approach are given in Section 4.

The wave propagation model uses a three-dimensional computational approach. This so-called “beam propagation method” (BPM) [7] does not rely on modal resolution of the optical beam, but rather calculates the evolution of the complete complex electric field. The primary advantage of this method is its ability to model arbitrary spatially dependent structures, such as refractive index (engineered or thermal), saturable gain, bend loss, material inhomogeneities, and a host of other effects, while at the same time allowing for arbitrary launch conditions. The output of the model describes the complete spatial profile of the (complex) optical field without having *a priori* knowledge of the modes of the fiber. The model numerically solves the paraxial wave equation with transparent boundary conditions to eliminate any real or induced reflections at the interface boundaries.

The BPM methodology had already been successfully applied to VLMA fibers [8], but required two changes in order to include thermal lensing and mode instabilities. The former was accounted for by changing the 3D refractive index profile according to the prescribed thermal lens. The inclusion of mode instabilities, however, required that the BPM effectively become time dependent. Computationally, this is simply not feasible for VLMA fibers. First, the spatial grid required for computation is already massive:  $200\mu\text{m} \times 200\mu\text{m} \times 5\text{m}$ . Second, the relative times of interest are orders of magnitude different. The optical time-of-flight down a 5m length of fiber is about 25ns. However, modal instabilities operate on a much shorter ( $\sim\text{ms}$ ) time scale. As such, comprehensive full-scale modeling would have required well over 10,000 full-fiber calculations before any real changes become evident. Even using the most sophisticated supercomputers, such a calculation would take many days to run, prohibiting any parametric analysis but the most rudimentary observations. Instead, a different path was explored in which the “steady-state” solutions were to be applied iteratively with discrete jumps in time that are significant compared to the time-of-flight down the fiber, but minute compared to the time scale of the dynamical instabilities under study. In this way, the full-scale BPM strategy could be applied to the dynamic problem while simultaneously minimizing computation time to a reasonable level suitable for studying the problem at hand. More details on this approach are given in Section 3.

Finally, it was noted throughout the program that even using the Blue Hive supercomputer at the University of Rochester, the simulations took exceedingly long periods of time to execute. For example, using our modified modal model to find the instability threshold for the simplest case studied (two modes in a  $20\mu\text{m}$  LMA fiber) would take 24 hours to complete using our fully allotted 24 nodes. Therefore, a methodology was developed to assess the viability of specific fiber designs *before* running the detailed simulations. Specifically, the data resulting from the bulk of our initial runs was used to generate a set of engineering rules for designing and down-selecting specific fiber types *without* using any propagation or thermal modeling. These engineering rules allowed us to eliminate non-viable solutions without wasting valuable computational resources, and focus on the development of promising new VLMA fiber types. More details will be presented in Section 6.

It must be noted that throughout our analysis, the fiber types analyzed were focused on conventional-type fibers (including polarization maintaining fibers) using waveguide-based physics, i.e. no photonic crystal or photonic band-gap fiber types were investigated. Ultimately, such alternative fiber types become challenging to fabricate to

spec and are highly susceptible to packaging (i.e., bending) and external thermal influences.

### 3. Beam Propagation Model Development

One of the key aspects of the BPM model is its ability to indiscriminately propagate the entire complex optical field rather than relying on modal decompositions. We define this aspect as critical since the large-scale temperature changes inside the pumped fiber dictate that the cold-fiber modes are insufficient to describe the propagation of light down the fiber from a strictly perturbative perspective, as is commonly done in modally resolved models. This is particularly relevant since the temperature profile is not even constant along the length of the fiber, especially in the case of single-end pumping.

#### 3.1 Full BPM Model

Our BPM model numerically solves the paraxial wave equation for the optical (electric) field  $E$  along the propagation ( $z$ ) axis as

$$\frac{\partial E}{\partial z} = \frac{i}{2k_0 n_R} \nabla_T^2 E + ik_0 \left( \frac{n^2 - n_R^2}{2n_R} \right) E + \frac{1}{2} \left( \frac{g_0}{1 + |E|^2 / I_{\text{sat}}} \right) E \quad (1)$$

where  $E$  is the optical field, where  $k_0 = 2\pi/\lambda$ , and  $n_R$  is a reference refractive index. On the right hand side of Eq. (1), the first term represents diffraction, and the second term accounts for the refractive index profile,  $n(x,y,z)$ , in three dimensions, including the engineered cross-sectional fiber profile (constant in  $z$ ) and the thermal contribution. The last term incorporates the spatial dependence of the gain doping profile through  $g_0(x,y)$  and accounts for spatially localized saturable gain in three dimensions.  $I_{\text{sat}}$  is the saturation intensity obtained including the influence of pump saturation [9] through a standard ytterbium (Yb) kinetics model [10].

Eq. (1) is solved with a finite-difference scheme (FD-BPM) [11] using the Alternating Direction Implicit (ADI) method [12]. The need to model long propagation lengths required that transparent boundary conditions be implemented to eliminate any real or induced reflections at the interface boundaries [13].

As stated earlier, the methodology for applying the BPM to the dynamic thermal model is to iteratively calculate the optical and thermal properties of the amplifier. First, the speed-of-light (ns-scale) propagation of the optical beam is calculated through the fiber using Eq. 1. Then, the full 3D thermal profile in the fiber is calculated using the standard 2D time-dependent heat equation at each cross-sectional step along the fiber using heating that is spatially defined via the pump/signal energy deposition/extraction. The dimensional reduction (3D to 2D) is reasonably valid due to the adiabatic nature of the *average* thermal evolution along the fiber, and reduces computation time significantly. This two-step process (optical / thermal) is repeated on thermal ( $\mu\text{s}$ ) timescales in order to simulate the dynamics represented by the thermal mode instability.

Reasonably early in the program, the results indicated that the computation is too memory intensive and insufficiently fast for anything but a few singular demonstrative simulations. The computation grid was approximately  $200 \times 200 \times 250,000 = 10$  billion data points each in optical amplitude, optical phase, and temperature (which must be



retained from one iteration to the next). Although it was initially suspected that the temperature grid could be reduced by a significant fraction ( $\sim 100\times$ ), it was recognized that this would only be true if one considers only the two lowest-order modes for a low numerical aperture ( $NA = 0.06$ ) geometry. Since some of our fiber concepts indicated that the second ( $LP_{11}$ ) mode is effectively nonexistent and others require the use of higher NA cores, neither of the requirements above are met universally, and the entire grid must therefore be calculated (and retained) in general. As such, all data must be kept at the 3 x 10B data size, which is simply prohibitive.

### 3.2 Reduced BPM Model

Two methods for minimizing the computation time and data volume were investigated. The first method was reducing the spatial grid (both transverse and axial since they are effectively coupled in order to produce accurate BPM results). If, for example, a factor of 5 can be gained in each of the three dimensions, then the three arrays (optical amplitude, optical phase, and temperature) can be reduced to 80M data points each, which would represent a viable data volume for the required exchange. Using this approach, however, appropriate care must be taken to ensure preservation of all beat lengths for proper validity of the model.

In the cases that were modeled using reduced-grid conditions, it was discovered that although reducing the resolution sufficiently to allow reasonable data sizes and computation time resulted in data that reproduced similar physical behavior under certain conditions, it was sufficiently inaccurate for use as a predictive tool for designing and engineering new fiber types, even using focusing on the  $LP_{01}$  and  $LP_{11}$  modes. As a simple example, the amplifier efficiency should not change considerably under dynamically instable conditions compared to stable, continuous-wave (CW) operation. However, in some cases that were modeled with a meaningfully reduced spatial grid, the amplifier efficiency was too high to be physically realistic. Due to this and other observed inconsistencies and inaccuracies, reducing the spatial grid resolution was deemed as a non-viable option for minimizing data volume and computation time.

The next path attempted was to implement a simplified thermal predictor model that would not require the storage and transfer of huge data volumes. In general, thermal effects are included in the model via induced change to the 3D refractive index profile according to the differential form  $\Delta n(x,y,z) = (dn/dT)\Delta T(x,y,z)$ , where  $dn/dT$  is the change of the refractive index of glass with respect to temperature ( $\sim 10^{-5}/^{\circ}\text{C}$ ). The localized temperature change  $\Delta T(x,y,z)$  is essentially driven by energy exchange between the pump and signal photons within the medium, and is conventionally calculated via the heat equation. The heat load that drives these thermal changes is given by  $(1-\eta_{\text{QD}})P_s(\sigma_e N_2 - \sigma_a N_1)$ , where  $(1-\eta_{\text{QD}})$  is the quantum defect,  $P_s(x,y,z)$  is the spatially resolved signal power,  $\sigma_{e/a}$  is the emission/absorption cross section at the signal wavelength, and  $N_{2/1}(x,y,z)$  is the spatially resolved upper/lower state electron density. Note that the non-radiative decay ( $N_2/\tau_2$ ) has been neglected for simplicity since its impact should be negligible in a high-efficiency amplifier.

This formalism can be further simplified by recognizing that  $(\sigma_e N_2 - \sigma_a N_1)$  represents the localized gain profile. In this case, the heat load can then be simplified as  $(1-\eta_{\text{QD}})P_s(x,y,z)g(x,y,z)$ , where the spatial dependence has been explicitly shown. Since the optical profile is directly linked to the heat load through the equation described above,

this means that the heat load will change before the heat can be redistributed. As a coarse approximation, this means the temperature profile may be considered to be nearly equivalent to the heat load for the purpose of implementing our serial BPM scheme.

Eliminating the calculation of the 3D temperature profile along the entire can result in significant savings in terms of computation time. However, the translation from heat load to temperature is a critical step that is omitted in the simplified formalism outlined above. Since conductive heat transfer is being ignored, straightforward conversion from heat to temperature will result in higher temperatures than expected, and the  $\mu$ s-scale diffusion implicit in the heat equation solutions will be absent. Implementing this approximation will therefore have an exaggerated impact on the optical field, which will then generate a substantially different heat load, resulting in a rapidly (and non-physically) varying thermal profile.

To mitigate this problem and emulate thermal diffusion, the process that was implemented consisted of mixing the newly generated thermal profile with the prior iteration thermal profile using a relative strength of  $\alpha < 1$ . The original idea was to determine the value of  $\alpha$  via merit function using an adiabatic requirement on the evolution of the thermal profile. However, we discovered through our simulations that adiabatic evolution of the temperature profile required a value of  $\alpha$  that was simply too low to generate mode instabilities. Instead, omitting the adiabatic requirement and using larger values of  $\alpha$  resulted in dynamic spatial instabilities. However, the thermal profiles in this case changed in an unphysical manner and were thus deemed unreliable from a physics perspective.

### **3.3 Final BPM Model Assessment**

The result of our efforts with the BPM modeling is that the method is either (a) too large and computationally intensive to represent anything other than a singular demonstration (which has already been published by other groups [14]), or (b) too inaccurate to produce meaningful trends or design validation. These findings therefore eliminate iterative BPM as a viable design tool for including the prediction of dynamic thermal mode instabilities.

## **4. Rate-Equation Model Development**

The basic modally resolved model separates the power and phase evolution of a given mode from its spatial field distribution. One of the fundamental drawbacks of this method is that the modes are fixed through the modeling by *de facto*, with only perturbative coupling between the modes to modify their behavior (power/phase), in order to facilitate rapid simulation. For the case of asymmetrically pumped high-power fiber amplifiers, this represents a flaw in using a modally decomposed model, and was our original motivation for attempting to apply the BPM methodology to this problem. However, we have developed a new method that overcomes this fundamental limitation while still retaining all of the benefits of modal decomposition modeling, as will be described in Section 4.2.

The rate equation modeling (REM) work started with an analysis of all relevant existing models. A dynamic model in particular was selected since non-dynamic models are incomplete by their very nature. While steady-state and stability-analysis type models are typically excellent at predicting trends, they are also notorious for requiring arbitrary fit parameters to match experimental data. Therefore, only dynamic models

were considered. Although many REM models exist (e.g., DTU, Jena, Clemson, AS Photonics, U. Mich., etc.), the model from the Air Force Research Laboratory (AFRL) [15] was down-selected as our initial starting point. AFRL's modally decomposed REM not only includes all of the relevant physics in a true dynamic model, but it does so in a transparent (physics-ready) methodology derived from fundamental (Maxwell's) equations. Perhaps most importantly, it allows modification for inclusion of higher-order physics. It is also very similar to our existing steady-state modally decomposed REM model and allows for simpler coding transition.

#### 4.1 Basic REM Model Definition and Validation

Modal propagation down the fiber amplifier, incorporating coupling between modes due to refractive index perturbations and amplifier gain, is described by the singular and deceptively simple equation

$$\frac{dE_j}{dz} = \sum_k \left[ ik_0 \kappa_{j,k}^{\delta n}(z) + \frac{1}{2} \kappa_{j,k}^g(z) \right] E_k(z) e^{i(\beta_k - \beta_j)z} \quad (2)$$

where  $E_i$  is the complex field of the  $i^{\text{th}}$  mode, and  $\beta_i$  is its propagation coefficient. Apart from the summation over all modes, Eq. 2 looks similar to a single-mode propagation equation where the kappas take the place of index and gain respectively. Their mathematical forms are given by

$$\kappa_{j,k}^{\delta n}(z) = \iint \Phi_j^*(x,y) \delta n(x,y,z) \Phi_k(x,y) dx dy \quad (3)$$

$$\kappa_{j,k}^g(z) = \iint \Phi_j^*(x,y) \left[ \sigma_s^e N_2(x,y,z) - \sigma_s^a N_1(x,y,z) \right] \Phi_k(x,y) dx dy \quad (4)$$

where  $\Phi_k(x,y)$  is the power-normalized spatial mode profile,  $\delta n(x,y,z)$  is the modification to the base refractive index (embedded in  $\beta$ ),  $\sigma_s^{e/a}$  are the emission/absorption cross-sections,  $N_{2/1}(x,y,z)$  are the excited/ground state population inversion densities, related to the total doping density via  $N_T(x,y) = N_2(x,y,z) + N_1(x,y,z)$ .

For the case of only a single mode, Eq. 3 represents a modification to the propagation coefficient  $\beta_j$ , Eq. 4 represents gain, and Eq. 2 reduces to the familiar propagation equation. In the multimode case, this still holds true for the  $j = k$  terms, however there exist cross terms that determine the coupling between modes. As in conventional waveguide theory, this coupling is determined by the spatial overlap of the two modes over the region of the perturbation, in this case the modification to the refractive index and the material gain. Note that the gain and index change over the length of the fiber, resulting in coupling coefficients that are  $z$ -dependent.

The time-dependent heat equation is solved between iterations of the optical solutions to determine the refractive index perturbation  $\delta n(x,y,z)$  at each point along the fiber. The populations  $N_{2/1}(x,y,z)$  are determined by spatially dependent ytterbium kinetics rate equations using the spatial distributions of the signal and pump power at each point along the fiber. The pump power is assumed to be spatially uniform and is calculated via the spatially integrated populations.

Although the model does not contain noise to initiate the instability, it is in fact not required. No practical seed launch into the amplifier is 100% efficient in launching

into the fundamental mode of the fiber, and power will be injected (unintentionally) into other modes of the fiber. Even if small, the seed power injected into other modes will dominate quantum noise (spontaneous emission), thus obviating the need for inclusion of noise in the model.

The model was validated by simulating fiber amplifiers two meters in length with a 20 $\mu\text{m}$  core diameter and a 230 $\mu\text{m}$  pump cladding. The nominal (room temperature) cladding refractive index was taken to be 1.45 with a core NA of 0.06. The doping density of the core was taken as  $6.2 \times 10^{25} \text{ m}^{-3}$ , with pump and signal wavelengths of 975 nm and 1080 nm, respectively. Other parameters were nominally selected for a convectively cooled Yb-doped silica fiber. The axial/temporal step size was determined to sufficiently resolve the mode beating while simultaneously ensuring conservation of energy in the system. Although smaller step sizes were also investigated, the results were similar but at the expense of additional computation time.

Though the model describes the coupling between all supported fiber modes, coupling between the fundamental and the next highest order mode is the strongest and thus will determine the thermal most instability (TMI) threshold in standard (step-index) fiber types. For this kW-class amplifier, 35 W of signal power was seeded into the fundamental ( $\text{LP}_{01}$ ) mode, with 1.75 W (5% of the fundamental-mode power) launched into the higher-order ( $\text{LP}_{11}$ ) mode. The pump was co-propagated with the signal launch.

Figure 1 shows the power evolution along the length of the LMA fiber amplifier of the  $\text{LP}_{01}$  and  $\text{LP}_{11}$  modes at sequential steps in time for several pump powers. At 750 W pump power, the amplifier shows stable behavior at all times (noted by the fact that the  $\text{LP}_{01}$  and  $\text{LP}_{11}$  curves are all identical for each time step, as indicated in the plot), with the  $\text{LP}_{01}$  mode containing most of the optical power. At 850 W pump power, modal power interchange along the fiber occurs and is dynamic, noted by the fact that the modal curves representing the various time steps are not identical. At 950 W pump power, the modal power transfer initiates earlier along the fiber, indicating a stronger instability.

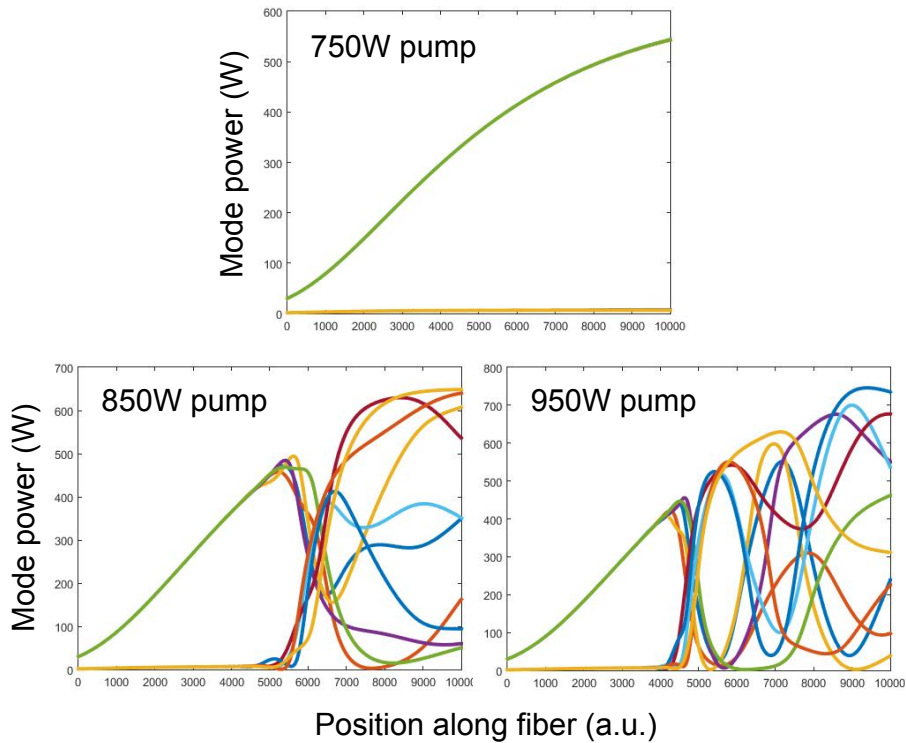


Figure 1:  $LP_{01}$  and  $LP_{11}$  power evolution along the fiber amplifier length at various steps in time. The seed power is 35 W and the pump power is show in each figure inset. Various time steps are shown as additional curves in the plots, with the  $t = 0$  case shown as green and yellow for the  $LP_{01}$  and  $LP_{11}$  modes respectively.

Figure 2 shows the temporal evolution of the power in each mode ( $LP_{01}$  and  $LP_{11}$ ) at various pump powers. Each simulation starts with a dynamic power transfer between the modes that, when under the instability threshold, stabilizes to CW-type conditions within 30 ms; this represents the settling time of the simulation and is dependent on the initial thermal profile selected. As the pump power is increased, the results indicate the *tendency* towards instability as the settling time (to CW-type conditions) becomes larger with increasing pump (and thus output) power. Dynamic instability is finally reached in the range 750-800W pump power, beyond which the power exchange does not stabilize.

The minute fluctuations near threshold (see the blue curve at 750W pump) are key for validating the (temporal) length of runs required, as the rapid power transfer between modes ceases below the instability threshold, but can be observed as threshold is approached.

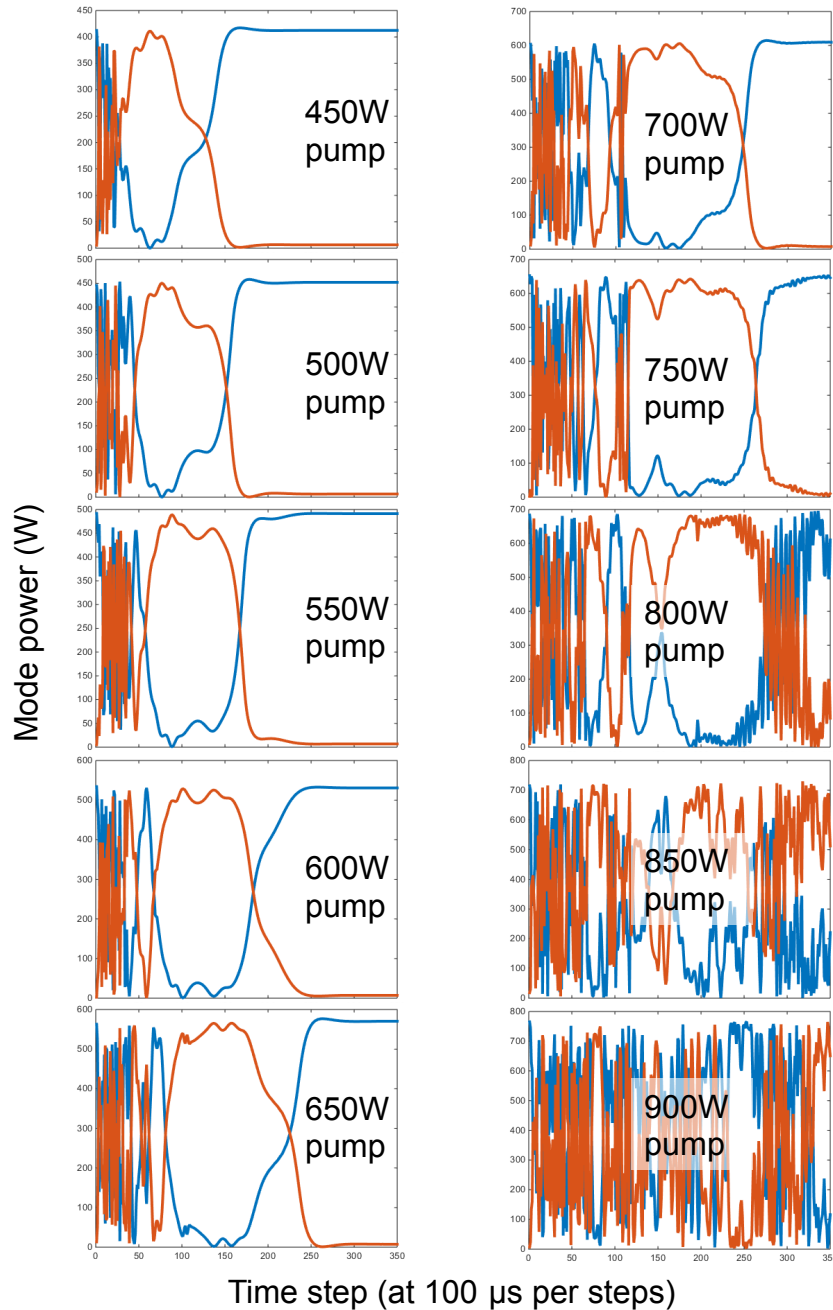


Figure 2:  $LP_{01}$  (blue) and  $LP_{11}$  (orange) power at the amplifier output as a function of time over a 35-ms time span. The seed power is 35W and the pump power is inset in each plot.

Similar runs were executed for various seed powers, resulting in the (coarse) instability thresholds shown in Fig. 3. The data shows that the instability threshold increases with seed power, which is not only physically justifiable (due to the increased saturation by the fundamental mode) but was also previously predicted [15].

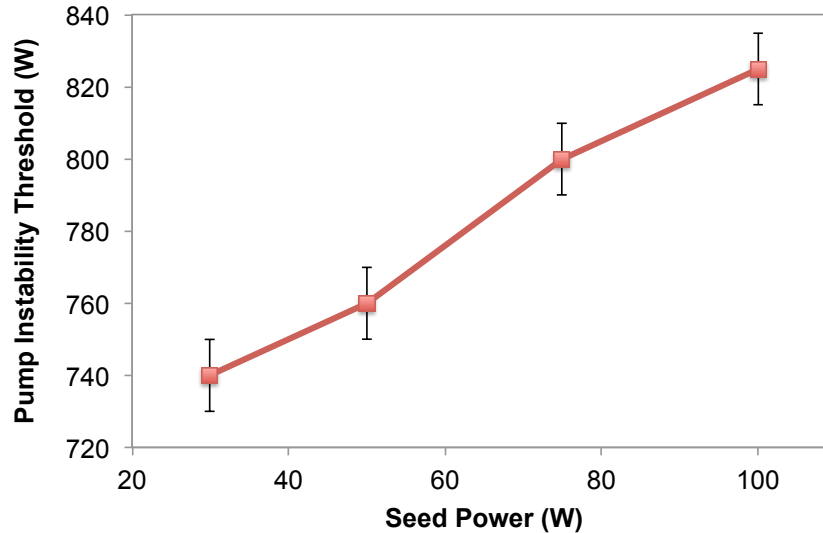


Figure 3: Threshold pump power for the onset of thermally induced mode instability as a function of seed power.

The results of Figures 1-3 demonstrate that the base model as coded yields predictions that reproduce the requisite physics at a level that is sufficiently quantitative for fiber design and engineering of realistic high-power fiber amplifiers.

#### 4.2 Modification to the REM Model

As stated previously, the fundamental flaw of using modally resolved models for our application is that the mode and its eigenvalue ( $\beta$ ) are fixed throughout the entire simulation space (both in time and along the length of the fiber). However, the varying thermal characteristic along the length of the fiber, given by Eqs. (2)-(4), means that the natural mode of the fiber (i.e., the ideal waveguide mode solution) can also change as a function of the length along the fiber and in time as the thermal characteristic dynamically changes. Since the pump power varies along the fiber length, drastically different thermal profiles from one end of the fiber to the other will lead to different transverse index profiles along the fiber. This directly translates modes having different transverse profiles on opposite ends of the fiber.

Provided the thermal changes are sufficiently slow compared to the mode formation length, any given mode of the fiber will adiabatically change along the length of the fiber with minimal coupling between modes (solely due to the axial temperature changes, and not including transverse effects). It is precisely this effect that we add into our REM model. Specifically,  $\Phi_j(x,y)$  becomes  $\Phi_j(x,y,z)$ , and  $\beta_j$  becomes  $\beta_j(z)$ . Note that this not only impacts the coupling coefficients in Eqs. (3) and (4), but also the phase matching condition in Eq. 2.

In this new formalism, we calculate the modes of a given fiber as a function of temperature, which manifests in the well-known graded-index profile for cylindrical symmetries [16]. The sets of modes (one set of unique transverse modes at each temperature) are solved using an existing finite-element-analysis (FEA) mode-solver. In this way, any given mode (e.g., LP<sub>01</sub>, LP<sub>11</sub>, etc.) has both a spatial profile and a propagation coefficient that vary (discretely) as a function of core temperature.

These results are applied to the REM model as follows: once the spatial temperature profile is calculated at a given point in the fiber, the resulting average core temperature is used to interpolate (a) the shape of each mode at that point in the fiber (using the previously solved mode set) and (b) their propagation coefficients  $\beta_i$ . Akin to the adiabatic physics in the actual (physical) fiber amplifier, adiabatic conversion with propagation is assumed such that the power does not transfer between modes; rather the mode's spatial profile and effective index change as the mode propagates down the fiber without transfer of power to any other modes (neglecting transverse effects). In this way, the evolution of the mode shapes and the beating between the modes are taken into account in a natural and physical way, and the remaining (transverse) thermal perturbations can be truly perturbative.

Figure 4 shows lineouts of the  $LP_{01}$  and  $LP_{11}$  modes calculated for both a standard  $25\mu\text{m}$ , 0.06-NA LMA fiber and a similar fiber with  $50\mu\text{m}$  core diameter. Each plot shows the overlap of many modes at different (peak) core temperatures ranging from 0 to  $900^\circ\text{C}$  above ambient. For this relatively small step-index fiber, the mode shape is only very weakly impacted (compressed) by the approximately parabolic temperature profile rising in the core at high powers.

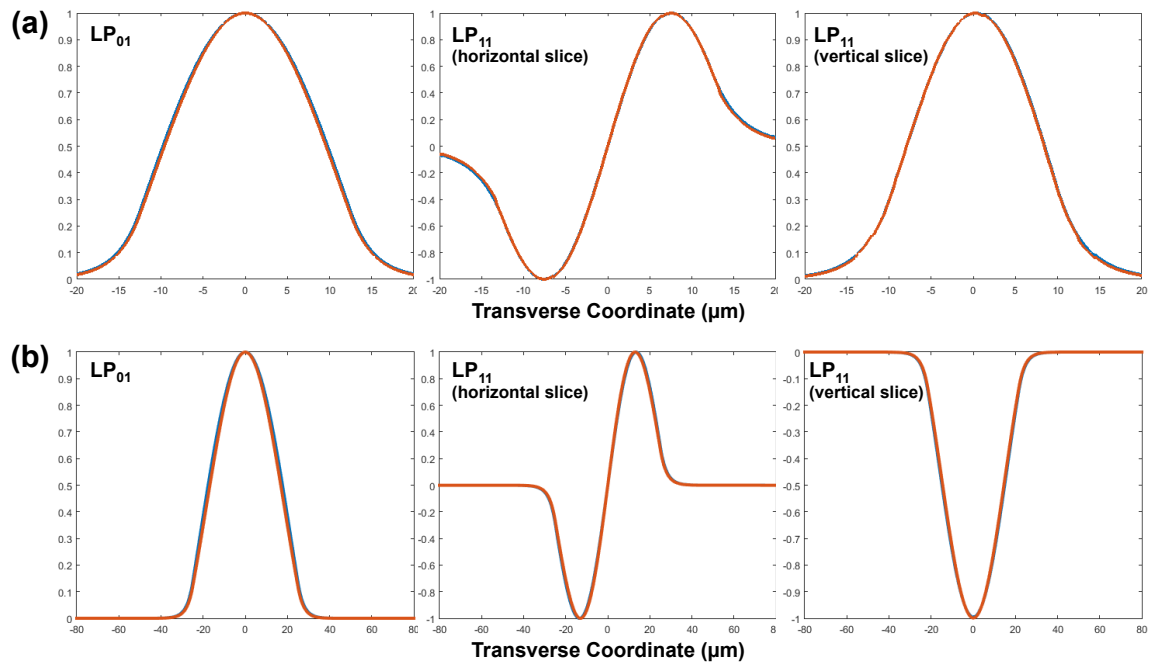


Figure 4:  $LP_{01}$  and  $LP_{11}$  mode lineouts for 0.06 NA fiber cores with diameter of (a)  $25\mu\text{m}$  and (b)  $50\mu\text{m}$ . Multiple curves on each plot range from 0 (blue) to  $900^\circ\text{C}$  (orange) peak temperature above ambient.

Figure 5 shows the difference in the effective index between the  $LP_{01}$  and  $LP_{11}$  propagation modes as a function of temperature for the same  $25\mu\text{m}$  and  $50\mu\text{m}$  fibers. It is important to note that for both fibers, the increased thermal load actually causes an *increase* in the separation of the mode eigenvalues, which would nominally lead to a decrease in the phase matching [see Eq. (2)]. Although the relative increases are small (2.2% for the  $25\mu\text{m}$  core, and 5.4% for the  $50\mu\text{m}$  core), the additional complications in



the simulation make the results more reliable for use in the development of new VLMA fibers.

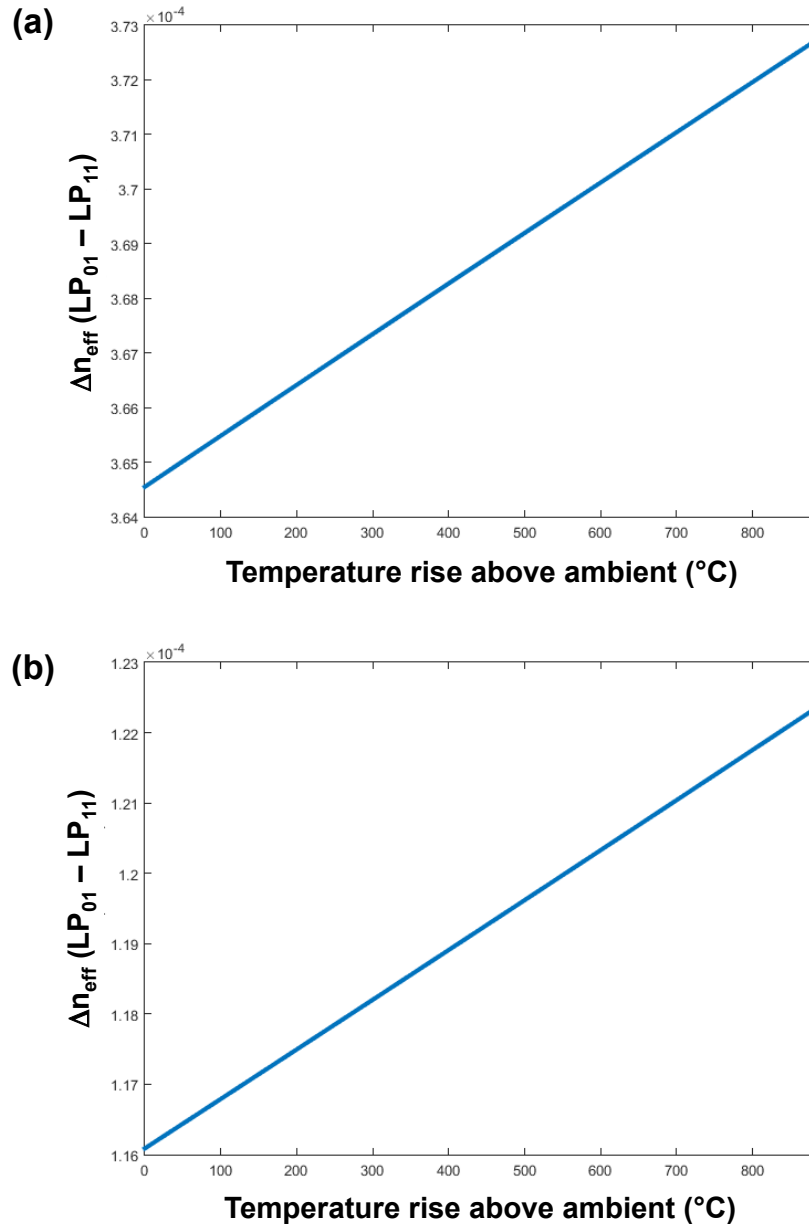


Figure 5: Effective index difference between  $LP_{01}$  and  $LP_{11}$  modes for 0.06 NA fiber cores with diameter of (a) 25  $\mu\text{m}$  and (b) 50  $\mu\text{m}$ .

The inclusion of the thermally varying mode profiles and propagation coefficients were subsequently used in all cases moving forward in order to provide a more accurate quantitative description of the physics resulting from the various fiber designs under consideration in the VLMA analysis.

## 5. Core Scaling with Conventional Step-Index Fibers

The REM model described in Sections 4 were applied to various fiber amplifiers to obtain a deeper understanding of the physics and understand the impact of thermal mode instability on core-area scaling. Unless otherwise stated, all parameters are the same as described in Section 4.

One interesting aspect allowed by the REM simulations is the ability to observe the transition between stable and unstable operation. Figure 6 shows a comparison of longitudinal temperature profiles taken 7  $\mu\text{m}$  off center of the fiber propagation axis over the last 8 mm of the fiber. The below-threshold curve shows a periodic-type temperature variation, indicating interferometric beating (without power exchange) between the high-power  $\text{LP}_{01}$  and low-power  $\text{LP}_{11}$  modes. In contrast, the above-threshold curve shows a much more complicated temperature profile, indicating significant modal coupling.

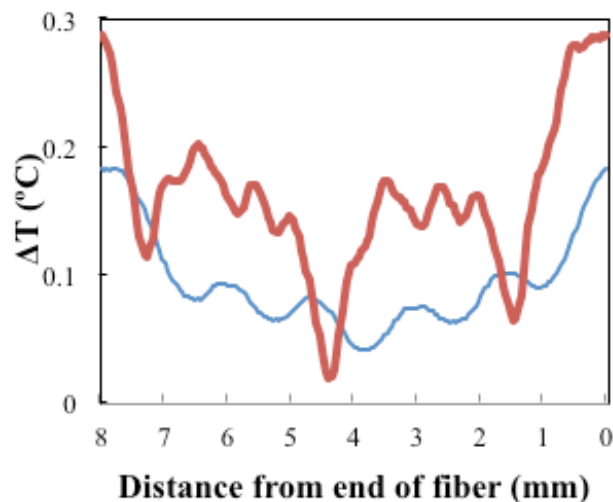


Figure 6: Temperature variation above the local temperature 7  $\mu\text{m}$  off the center of the fiber axis. Blue and red curves are below and above threshold, respectively.

### 5.1 Core-Diameter Scaling

The nature of TMI is insidious in that even though beam quality can be retained at low power, LMA fibers driven to higher powers exhibit thermally induced mode instability [17] that is characterized by a significant fraction of optical power being exchanged between modes of the fiber at kHz rates. To date, some methods have been demonstrated to reduce the impact of TMI and increase its threshold [18], which again leads to the exploration of fiber amplifiers with larger core areas. It is therefore prudent to understand what happens to the TMI threshold when the core area is increased for conventional step-index fiber. Although some preliminary modeling on step index fibers has been carried out [19], the work used a significantly simplified model that while saving computation time, neglected critical physics such as transverse spatial hole burning which is at the core of TMI physics. Moreover, the results are dependent on an arbitrary frequency difference between the modes that not only obscures the analysis, but is also unphysical from the perspective of realistic launch conditions.

The REM model was applied to fibers with core diameters varying from 20 to 50  $\mu\text{m}$ , each with 230 $\mu\text{m}$  cladding diameter. The doping density of the core was adjusted between 2.5 and 6.2  $\times 10^{25} \text{ m}^{-3}$  to maintain the same fiber length and output power for a given pump power as the core diameter is adjusted. Simulations were run with 25 W increments in pump power, and the TMI threshold was determined when dynamic power exchange between modes was observed (as shown in Fig. 2).

Figure 7 shows the resulting TMI threshold for core diameters ranging from 20  $\mu\text{m}$  to 50  $\mu\text{m}$  for forward a forward-pumped amplifier. The error bars indicate the 25 W pump power increment. Figure 8 shows a monotonically decreasing TMI threshold with increasing core diameter. At first glance, this may seem counter intuitive since the heat is generated over a larger area. However, thermal effects (specifically thermal lensing) have been observed to have larger impact on larger core diameters [20], a fact that has also been confirmed via analytic and numerical modeling [21].

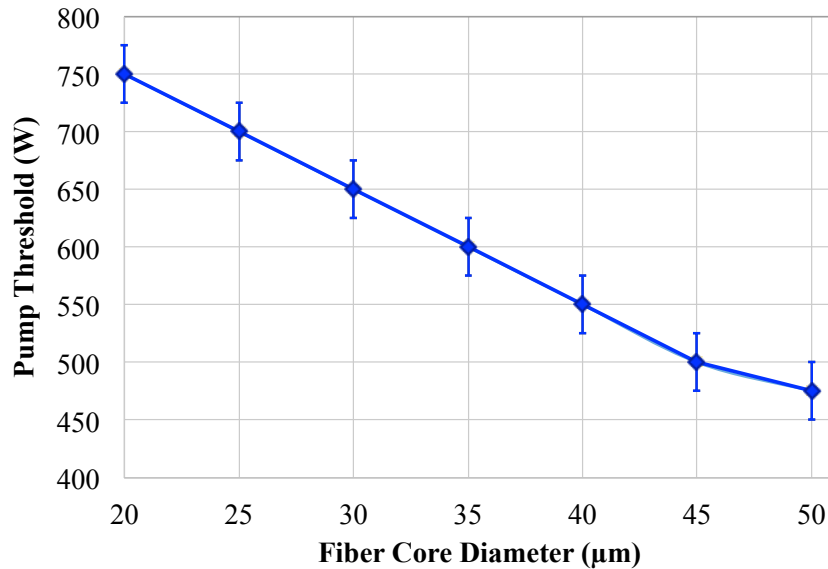


Figure 7: TMI threshold for forward pumped LMA fiber as a function of core diameter. The line is a guide for the eye, and the error bars represent the 25 W pump increment.

The trend observed in Fig. 7 means that even though TMI currently represents a challenging in power scaling LMA fiber amplifiers, it also represents a significant barrier to increasing the core diameter for mitigating nonlinear effects unless other methodologies are brought in to combat TMI. This will be the focus of the remainder of this work. As such, Fig. 7 is not only valuable in physical understanding of the phenomenon, but also in comparing new fiber designs to conventional step-index fiber.

## 5.2 Pumping Considerations

Since the thermal issues resulting in TMI are due to heat distributed by pump absorption, it is natural to consider the impact of pump geometry on the TMI threshold. Figure 8 represents the typical case of forward pumping (i.e., co-propagation the pump and signal light). Notionally, this places a large heat burden towards the input end of the fiber. The opposite case, backward pumping (i.e., counter-propagating the pump and signal light)

places a large heat burden towards the output end of the fiber. Therefore, one may consider that backward pumping will not result in any improvement (i.e., increase in TMI threshold). However, if we instead consider distributing the heat burden throughout the fiber, for example by including both forward and backward pumping, then it may be reasonable to expect an improvement to manifest as increase in the TMI threshold.

Figure 8 shows the temperature distribution as a function of length along the fiber for three cases: forward pumped, backward pumped, and bi-directionally pumped. The bi-directional pumping scheme was specifically designed to flatten out the temperature curve as much as possible with the goal of increasing the TMI threshold.

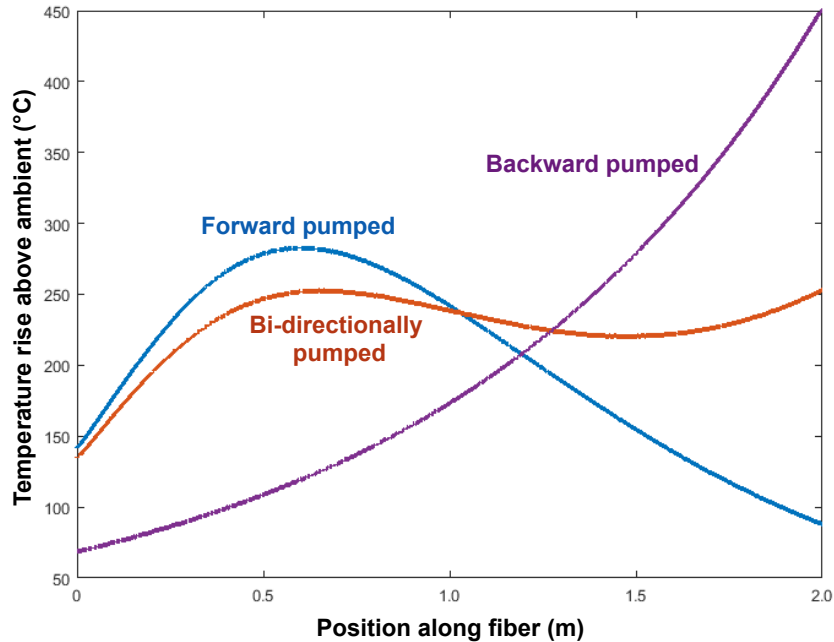


Figure 8: Thermal distribution along 25- $\mu\text{m}$  LMA fiber for forward (blue), backward (orange), and bi-directional (purple) pumping.

Figure 9 shows the  $\text{LP}_{01}$  power along the length of the fiber at the TMI threshold for each case. As might be expected at TMI threshold, the mode instability occurs within the fiber where the temperature reaches its highest point. For the bi-directionally pumped case, although the temperature profile is relatively flat, its peak temperature occurs only a little further along the fiber than for the forward-pumped case and thus the modal power exchange occurs only a little farther down the fiber (albeit at higher pump power).

The flatness of the bi-directionally pumped case, however, does have its benefits. One can immediately see from Fig. 9 that the temperature peak in the bi-directional case is lower than that of the forward pumped case. It stands to reason that the TMI threshold would be correspondingly higher, which was borne out numerically. Figure 10 shows the results for the three pumping cases. In the bi-directionally pumped case, the fraction of forward/backward pumping was optimized at each core diameter to provide the flattest thermal profile along the fiber.

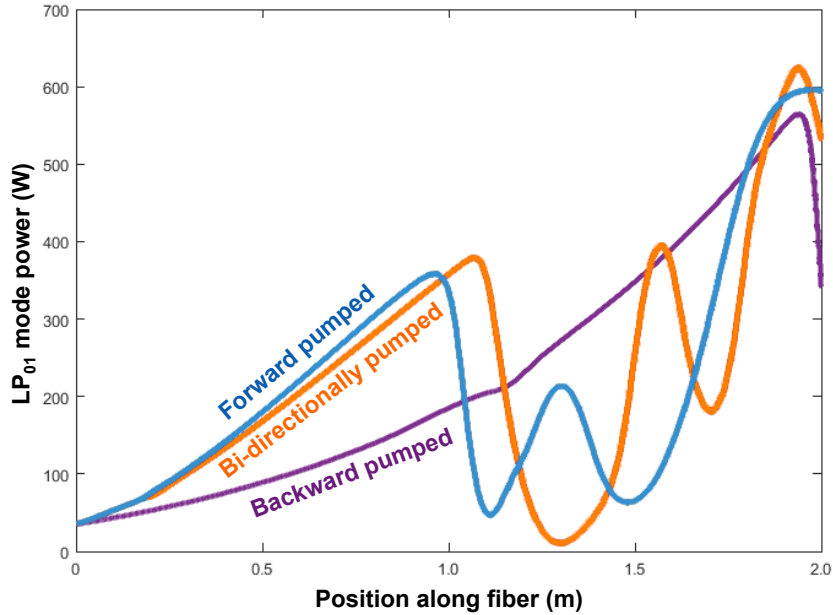


Figure 9:  $LP_{01}$  mode power distribution along  $25\mu\text{m}$  LMA fiber for forward (blue), backward (orange), and bi-directional (purple) pumping, at their respective TMI thresholds.

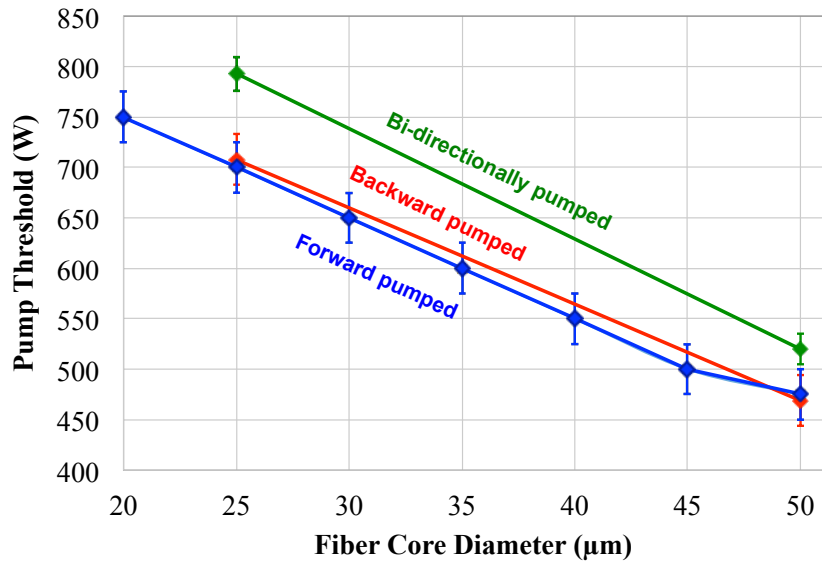


Figure 10: TMI threshold for forward (blue), backward (red), and bi-directional (green) pumping as a function of core diameter. The lines are guides for the eye, and the error bars represent the pump increment.

Although the backward-pumped case does not provide any benefit due to the very high temperatures at the end of the fiber, the bi-directionally pumped case offers a  $\sim 10\%$  increase in the TMI threshold. Even though in itself this benefit is not substantial, it may be more beneficial when combined with other TMI-mitigation methods. Note that this improvement is less than that predicted using the BPM method [22], although the initial conditions for those simulations were not stated. Other researchers have investigated

double passing the *signal*, in both amplifier and laser configurations, and found a reduction in the TMI threshold in both cases compared to that of the single-pass amplifier [23].

The results of this section make it abundantly clear that new methods for scaling the core area of LMA fibers need to be developed. This will be the focus of the remainder of the document.

## 6. Novel VLMA Fiber Designs

The results of the prior section demonstrate that it is critical to seek new fiber designs for core-area scaling. Nominally speaking, the analysis of VLMA fibers can proceed straight forwardly using the REM model. However, computational resources set practical limits on what can be achieved in a reasonable amount of time. Specifically, a single set of two-mode-only runs with ramped pump power, each with sufficient time to observe modal instability and its potential stabilization, (i.e., one set of runs to determine the instability threshold) requires ~24 hours of run time exploiting 120 processors on 24 nodes using the University's Blue Hive supercomputer. In addition, certain designs require multiple mode pairs (e.g. LP<sub>01</sub>-LP<sub>11</sub>, LP<sub>01</sub>-LP<sub>02</sub>, etc.) to be investigated to determine which mode has the lowest instability threshold. Therefore, preliminary assessment methods have been developed to minimize computation time.

Although the program was originally stated to explore only conventional step-index fibers using gain filtering (confined gain), inclusion of further index profile engineering was viewed as a significant opportunity not to be missed. Only conventional index-profiling designs were considered; photonic crystal fiber and photonic band-gap fiber were deemed outside the range of interest for this program.

Nominally, the target VLMA fiber has a 50 $\mu$ m effective core diameter with stable, diffraction-limited emission. We have developed several guidelines motivating our concepts and designs, which will be discussed below:

- (a) Significant HOM filtering – If HOMs have high loss relative to the fundamental mode, the instability threshold will be higher and stable beam quality will result. In other words, power seeded from the LP<sub>01</sub> mode to an HOM that experiences loss results in lower net effective mode coupling. The utility of this idea with respect to modal instabilities was experimentally proven by ARFL, and later numerically corroborated by AS Photonics. The first guideline is therefore to design waveguides with strong mode filtering of some kind. This is also viewed as the most challenging, since to date no such waveguides exist commercially beyond 25 $\mu$ m core diameter.
- (b) Large mode-index contrast – While the LP<sub>11</sub> mode is typically the most detrimental to LP<sub>01</sub> propagation in general, the small modal index difference between these modes leads to a large beat length and correspondingly significant phase matching, which are ripe conditions for initiating modal instabilities. By designing for larger spacing of effective indices between the LP<sub>01</sub> and the HOMs, the beat length will be shorter, reducing the phase matching. Alternatively viewed from the grating perspective, longer period gratings necessarily have fewer “reflections” per unit length that add coherently, necessitating a longer or stronger grating to generate the same effect. In addition, the longitudinal heat

flow (which we have experimentally measured as significant over cm-scale lengths in some cases [24]) should aid in diffusing shorter period gratings. The second guide is therefore to maximize the differential modal index between the fundamental mode and the pertinent HOMs (which may not be the LP<sub>11</sub> depending on the specific fiber design).

- (c) Reduced spatial overlap – The perturbative coupling that leads to modal instability depends on the spatial intensity overlap between the LP<sub>01</sub> and HOMs in the region of the (index) perturbation. By designing waveguides that sufficiently perturb the spatial profiles from the nominal (step-index) LP mode profiles, the spatial overlap and thus coupling between modes can be reduced, increasing the instability threshold. In addition, this joint mode overlap is only relevant in the regions of thermal perturbations, which are dictated by the gain distribution. The third guide is therefore to reduce the spatial (intensity) overlap between the LP<sub>01</sub> and the relevant HOMs particularly over the region that is doped with rare-earth ions (e.g., ytterbium in the case of interest to this program).
- (d) Reduced mode set – Nominally, the modal effective indices (whose difference govern the mode coupling) are bound between the core and cladding refractive indices. If designs can be reached that reduce the total number of modes within the same eigenspace ( $n_{\text{core}} > n_{\text{eff}} > n_{\text{clad}}$ ), then it will likely also increase the differential modal index [as desired per guideline (b)]. In addition, it will also reduce the number of degrees of freedom in the system, which should fundamentally lead to increased stability since there is less “noise” to seed the instability process (e.g., from imperfect seed launch). The fourth guide is therefore to reduce the total number of modes within a given NA space.

Note that nature provides various ways for several of these guidelines to work together. For example, modes that do not have significant spatial overlap [guideline (c)] are likely to have larger effective index contrast [guideline (b)] since the effective index is related to the spatial overlap between the optical field and the refractive index. In another example, using strong gain filtering (50-60% radial gain confinement) to cut out the LP<sub>11</sub> mode [guideline (a)] means that the next HOM will cause the problems; however, the next HOM will have a lower effective index [guideline (b)] and reduced spatial overlap [guideline (c)].

Many such candidates were conceptualized, modeled for spatial overlap and  $\Delta n_{\text{eff}}$ , and assessed using the REM model. The key successful design results are described in the following subsections.

### **6.1 Confined-Gain Fiber**

Confined gain has been recognized as one of the key methods for mode control in VLMA fibers, therefore conforming to guideline (a). Not only has it been well modeled [6,8], but it has been experimentally validated [25] including powers up to 300 W [26]. The key to “gain filtering” is not to introduce loss into the amplifier but rather to deny gain to HOMs under all circumstances. The physics of gain filtering using confined gain is best illustrated in Fig. 11.

Although the impact of confined gain on the TMI threshold was originally studied in the AFRL publications [15], the radial confinement was limited to 80% of the core

diameter. While the results still showed an increase in the TMI, the full potential of confined gain was not realized in those simulations. Theoretical studies [6,8] report that 50-60% of the core diameter represents the best modal suppression. Since filtering out HOMs necessarily results in a reduction of TMI tendencies (via increased threshold), it is prudent to optimize the effectiveness of gain filtering.

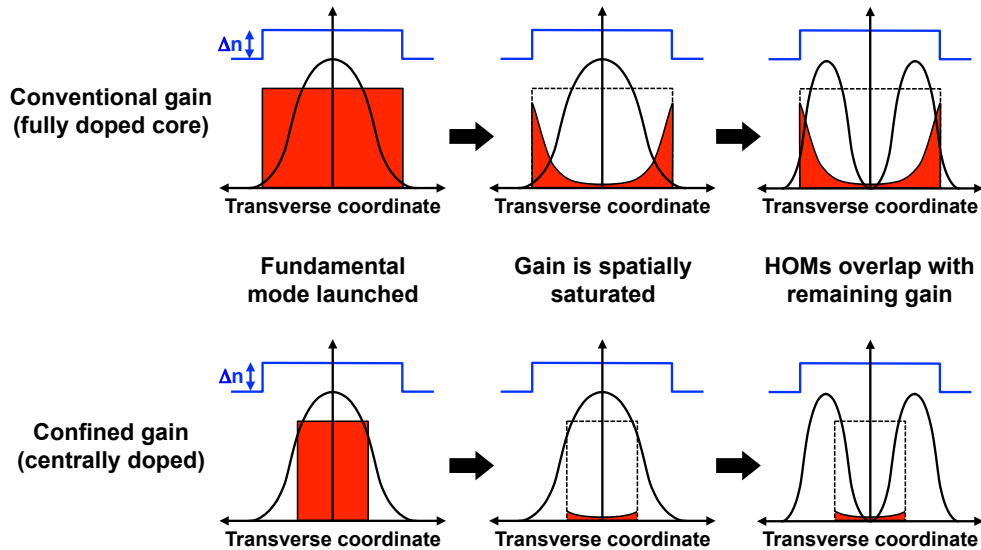


Figure 11: Conventional gain fibers (top) provide gain to HOMs especially when the gain is saturated. Confined gain (bottom) eliminates gain for HOMs even under saturation conditions.

In our simulations, we used a  $50\mu\text{m}$  core diameter with a 60% doping diameter. With the same cladding diameter, this represents the same approximate laser kinetics as a  $30\mu\text{m}$  LMA fiber core. It is important to note that confining the gain does not mean increasing the absorption length if the waveguide diameter is increased.

The results of the simulations were extremely encouraging. While stability was maintained up to 1kW of power, higher powers also resulted in another stability region. This means that at the very minimum, over a factor of two was gained in the TMI threshold for a  $50\mu\text{m}$  fiber. It is notable that *the TMI threshold for the  $50\mu\text{m}$  confined-gain fiber is at least 40% higher than the TMI threshold for a conventional  $25\mu\text{m}$  LMA fiber.* These results are captured in Fig. 12, where the confined-gain simulation shows both observed thresholds.

These extremely encouraging results necessitate further study of confined-gain fiber as a new platform for VLMA fiber types. In addition to continued power scaling, more modes need to be included in the study; since the  $LP_{11}$  mode is typically eliminated by gain filtering due to the null in the center of its intensity profile, the  $LP_{02}$  mode becomes the next threat to beam quality and mode stability.



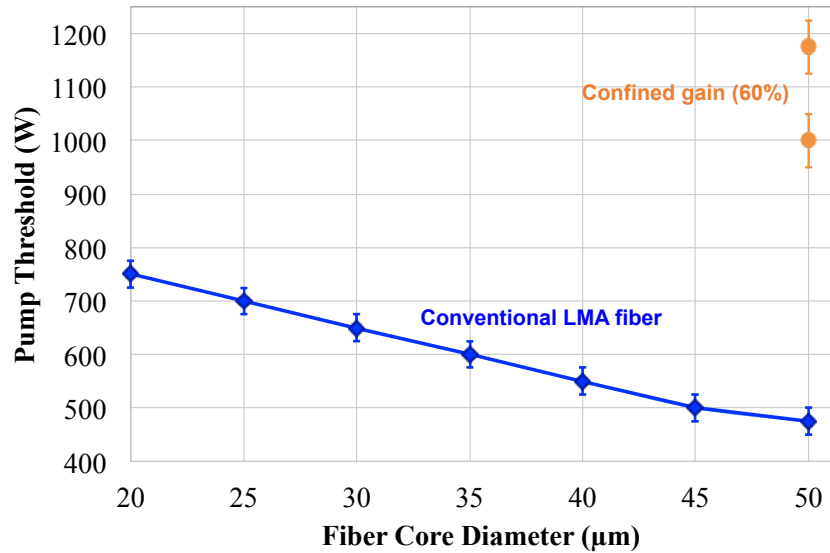


Figure 12: TMI threshold for confined-gain fiber (orange) compared to conventional LMA fiber (blue). The lines are guides for the eye, and the error bars represent the pump increment. The dual points for the confined-gain fiber are explained in the text.

## 6.2 Cladded Linear Index Graded (CLING) Fiber

In addition to gain tailoring, the concept of refractive-index profiling was also brought to bear in this program. In the simplest terms, waveguide modes are well represented by a quantum mechanical potential (i.e., a quantum well) viewed upside down. The eigenvalues (effective indices) are positioned in the “well” at an appropriate “energy level” (location in refractive index space), and the mode size is largely dictated by the location of the edges of the “well” (refractive index boundary). This concept is shown in Fig. 13(a). Note that the modes in this case are approximately the same size and thus have high spatial (intensity) overlap.

One method to reduce the overlap between the modes, in order to follow guideline (c), is to alter the shape of the “well”. Based on the above logic, it is reasonable to assume that if the “well” were tapered (i.e., a graded-index), the second mode would be larger than the fundamental mode. This concept is depicted in Fig. 13(b), and is oversimplified since the changes in  $n_{\text{eff}}$  were not taken into account. Nonetheless, the concept of modifying the waveguide profile to affect the mode sizes stands.

In studying this concept, the shape of the index profile was found to be important. Although only two modes are shown in Fig. 13, a VLMA fiber will by default have many modes, with the effective indices of the lowest modes gathered higher in the inverted index well. Designing a conventional parabolic graded index provided challenges since the relative LP<sub>01</sub>-LP<sub>11</sub> overlap was strongly dependent the precision to which the parameters were hit; a 5% change in the width of the waveguide resulted in a significant reduction in the desired size mismatch. With a linear index grade, the sensitivity to manufacturing tolerances was found to be significantly reduced; if both eigenvalues moved up or down the well, they largely did so together with a reasonably consistent overlap. A sub-linear index profile did not provide sufficient mode separation, much like the steep edges of a conventional step-index fiber.

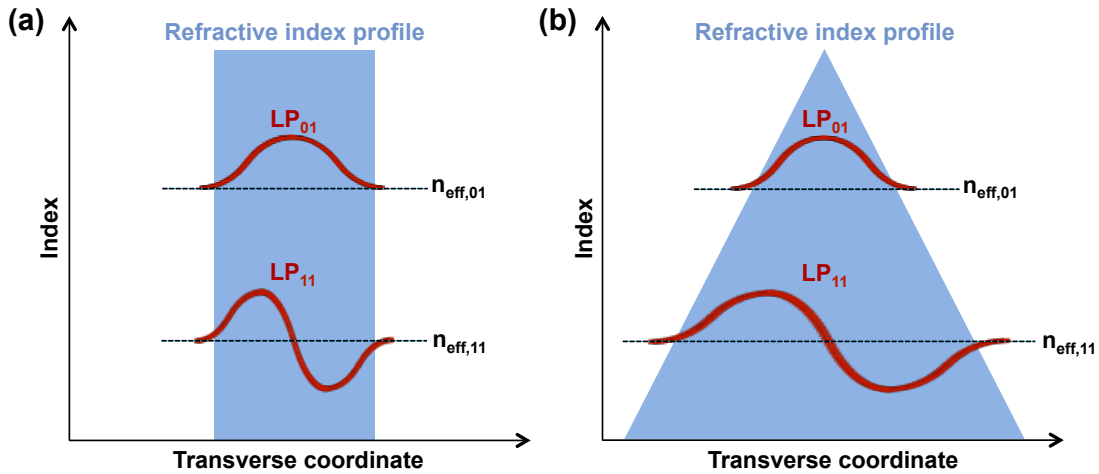


Figure 13: Comparison of modes between step-index and graded-index fibers. (a) Modes of a conventional step-index fiber are nearly the same size. (b) In contrast, modes of a graded-index fiber are not the same size, with higher-order modes being increasingly larger.

Therefore, due to both physics and tolerances, we settled on the **cladded linear index graded fiber**, or CLING fiber. The specific design we selected is shown in Fig. 14. The initial idea was to modify a conventional step-index fiber with a 0.06 NA by bumping the center up and the edges down by the same amount. The total core diameter was expanded to 100  $\mu\text{m}$  in order to allow sufficient expansion of the LP<sub>11</sub> mode.

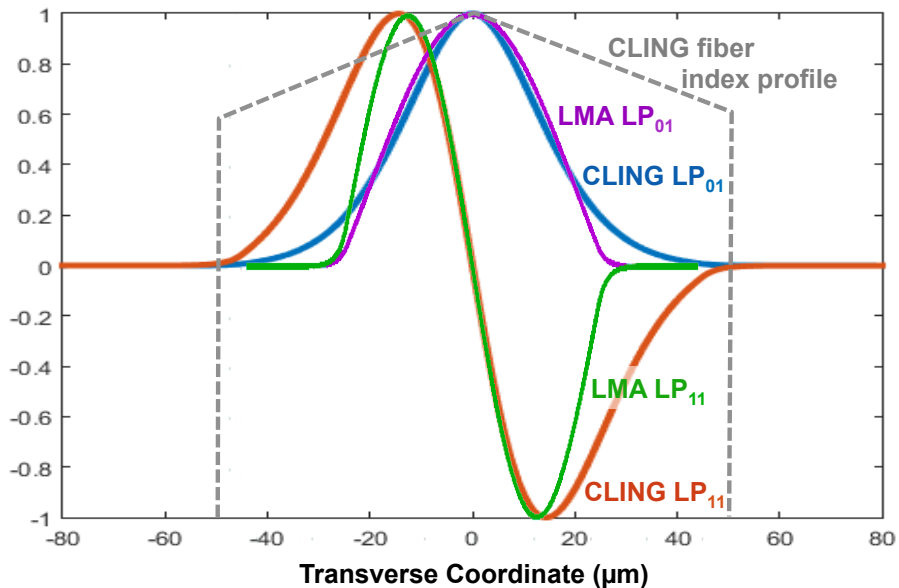


Figure 14: Modes of a LING fiber compared to modes of a conventional 50- $\mu\text{m}$  step-index fiber of the same average NA (0.06). The edge index step of the LING fiber is 0.0041 while the graded portion spans 0.0011.

Figure 14 shows both the LP<sub>01</sub> and LP<sub>11</sub> modes for two fibers having the same effective area for the fundamental mode: the CLING fiber (blue and orange, respectively)

and a 50 $\mu\text{m}$  LMA fiber (purple and green, respectively). Note that although the fundamental modes are approximately the same size and shape, the LP<sub>11</sub> mode of the LING fiber is substantially (almost 40%) wider. Radially, this means that the 2D overlap is reduced by nearly a factor of two, in principle significantly raising the TMI threshold.

Figure 15 shows the TMI threshold of the CLING fiber in comparison to the conventional step-index LMA fiber type. The CLING fiber shows a 68% increase in the TMI laser threshold over a conventional LMA fiber of the same fundamental mode size (50 $\mu\text{m}$  effective core diameter). Moreover, *the TMI threshold is higher than that of the industry standard 25 $\mu\text{m}$  LMA fiber, but with a mode area that is 4x larger.*

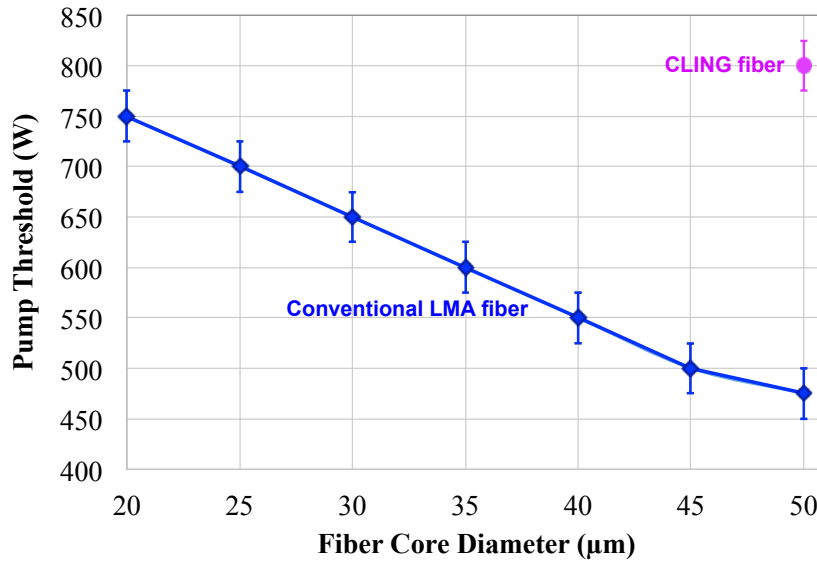


Figure 15: TMI threshold for CLING fiber (purple) compared to conventional (step-index) LMA fiber (blue). The lines are guides for the eye, and the error bars represent the pump increment.

The CLING fiber modeled here had a 50 $\mu\text{m}$  gain-dopant diameter in order to be similar to conventional LMA fiber. In spite of the difference in LP<sub>01</sub> and LP<sub>11</sub> mode sizes, the concept of gain filtering has not been fully applied here. Adding gain filtering to this concept would require a gain doping diameter of  $\sim 30\mu\text{m}$ , much smaller than what was used in the present simulations. Additional exploration and design of CLING fibers is highly recommended, particularly with the inclusion of gain filtering.

### 6.3 Trefoil Fiber

In an effort to meet both guideline (c) (reduced overlap) and guideline (d) (reduced mode set), a triangular core was considered. Although such a core could in principle be fabricated, exploiting conventional rod-in-tube or stacked-rod geometries are much more practical. Therefore, the geometry considered is that of three rods in what we call the Trefoil fiber. Each of the three cores has 0.06 NA, with a diameter selected to produce an effective area of the fundamental mode that is equivalent to a 50 $\mu\text{m}$  step-index fiber of the same NA.

The first three modes of the Trefoil fiber investigated are shown in Fig. 16. In this figure, the green lines represent the core boundaries, while the red ovals denote the location of power in the fundamental mode. One immediate success of this fiber type is

that the  $LP_{11,a}$  mode has at most a 60% spatial overlap with the  $LP_{01}$  mode. Perhaps more importantly, the degeneracy of the  $LP_{11}$  modes has been broken. The  $LP_{11,b}$  mode has a much lower overlap with the fundamental mode, near 30%. This means that in practice, only half of the power will be leaked out of the fundamental mode, which should result in not only better beam quality, but higher TMI threshold.

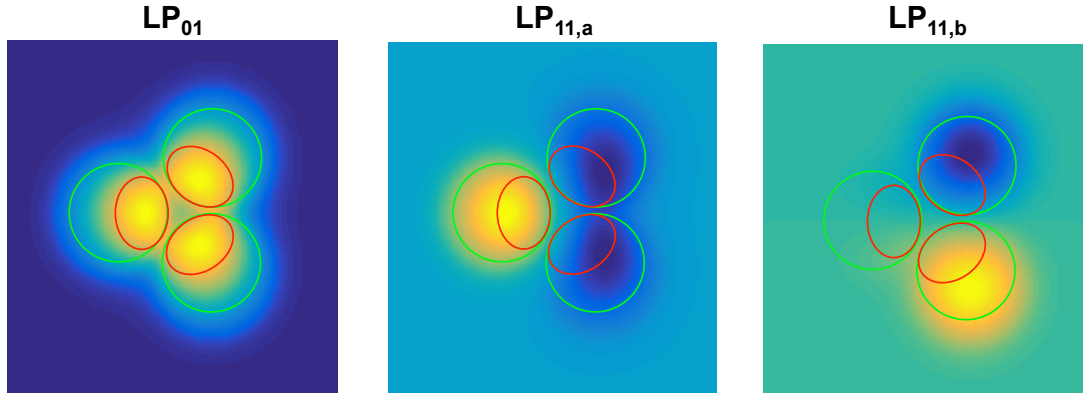


Figure 16: Lowest-order modes of a Trefoil fiber. The green circles annotate the core locations, while the red ovals are guides to the eye for marking the fundamental mode power.

Unfortunately, since the concept came late in the program, only a single set of TMI simulations were performed for this preliminary Trefoil fiber design, with the results shown in Fig. 17. The TMI threshold of 650W showed a promising 37% increase over the 50 $\mu$ m LMA fiber even for this un-optimized design. However, regions of stability were found at pump powers up to 875W. Given the reduced spatial overlap and the multiple regions of stability, additional exploration and design of Trefoil fibers is highly recommended, particularly with the inclusion of gain filtering and attention paid to the beam quality of the fundamental mode.

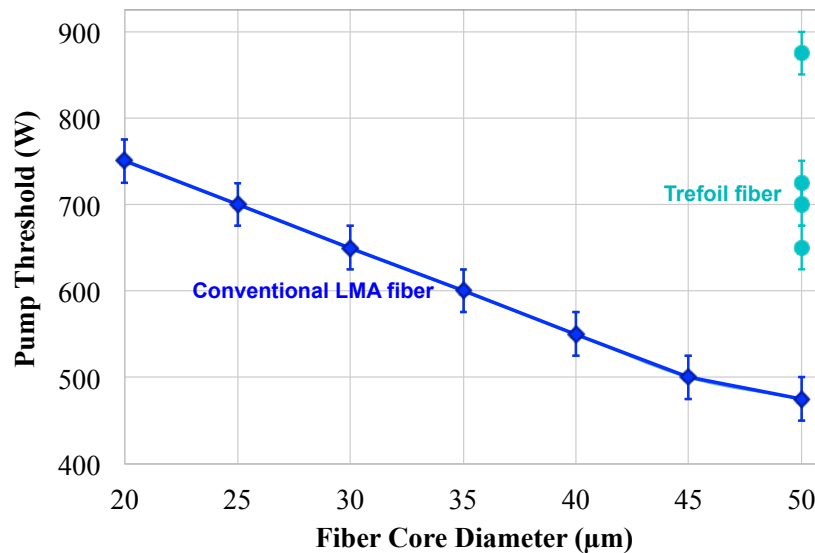


Figure 17: TMI threshold for Trefoil fiber (teal) compared to conventional (step-index) LMA fiber (blue). The lines are guides for the eye, and the error bars represent the pump increment.

## 7. Summary and Conclusions

Many different fiber types and designs were explored in this program using a validated rate-equation-based model for accurately modeling the beam quality in VLMA fiber amplifier while simultaneously including the effects of thermal lensing and thermal mode instability.

Mode-area scaling using conventional LMA fibers is simply not possible since the TMI threshold *decreases* with increased core area. Modifications in pump geometry can provide a modest benefit, particularly when flattening out the temperature profile along the fiber

Confined gain was studied and found to provide exceptional resilience to TMI (at least 2x increase in TMI threshold), as was originally proposed. Two new promising fiber types, CLING and Trefoil, were invented, and both exhibit features with modeled and expected resilience to TMI.

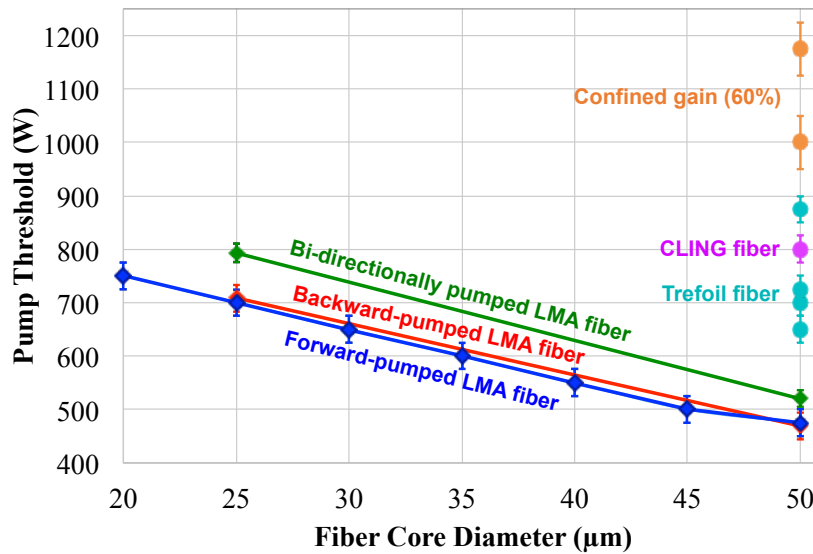


Figure 18: TMI threshold results summary for all conditions and fiber types. TMI threshold is shown for forward (blue), backward (red), and bi-directional (green) pumping as a function of core diameter. Also shown are the TMI threshold for the confined-gain fiber (orange), the CLING fiber (purple), and the Trefoil fiber (teal). Note that the regions of stability at higher pump powers were found for the confined-gain and Trefoil fiber types. The lines are guides for the eye, and the error bars represent the pump increment.

The most important results are captured in Fig. 18, which shows all of the calculated TMI thresholds together in a single plot, and Table 1, which quantifies and annotates the findings specifically for scaling to 50μm core diameter. It should also be noted that multiple effects can be integrated into a single design, such as using the CLING fiber with gain filtering (confined gain) and bi-directional pumping, for maximum TMI suppression.

Table I: Program summary results for 50 $\mu$ m effective core diameter fibers

Scaling method	TMI Threshold	Notes
LMA core scaling	37% decrease	Not viable – new fiber types needed
Backward pumping	No change	TMI occurs at hot (output) end of fiber
Bi-directional pumping	10% increase	Optimize to minimize temperature peak
Confined-gain fiber	>110% increase	Even higher power stability regions
CLING fiber	68% increase	No explicit gain filtering included
Trefoil fiber	37% increase	Un-optimized design, no gain filtering

Key results from this program will be presented at conferences and written up for publication in refereed journals. The program results will be summarized in a presentation at the HEL-JTO review during the 3<sup>rd</sup> week of May.

## 8. List of Symbols, Abbreviations, and Acronyms

ADI	alternating direction implicit
AFRL	Air Force Research Laboratory
BPM	beam propagation method
CLING	cladded linear index graded
CW	continuous wave
DEW	directed energy weapon
FD-BPM	finite difference beam propagation method
FEA	finite element analysis
HOM	higher order mode
LMA	large mode area
NA	numerical aperture
REM	rate equation modeling
TMI	thermal mode instability
VLMA	very large mode area

## 9. References

1. J. M. Fini, "Bend-resistant design of conventional and microstructure fibers with very large mode area," *Opt. Express* 14(1), 69–81 (2006).
2. R. C. G. Smith, A. M. Sarangan, Z. Jiang, and J. R. Marciante, "Direct measurement of bend-induced mode deformation in large-mode-area fibers," *Opt. Express* 20, 4436-4443 (2012).
3. F. Jansen, F. Stutzki, H.-J. Otto, T. Eidam, A. Liem, C. Jauregui, J. Limpert, and A. Tünnermann, "Thermally induced waveguide changes in active fibers," *Opt. Express* 20, 3997-4008 (2012).
4. B. Ward, C. Robin, and I. Dajani, "Origin of thermal modal instabilities in large mode area fiber amplifiers," *Opt. Express* 20, 11407-11422 (2012).
5. Z. Jiang and J. R. Marciante, "Impact of transverse spatial-hole burning on beam quality in large-mode-area Yb-doped fibers," *J. Opt. Soc. Am. B* 25, 247-254 (2008).
6. J. R. Marciante, "Gain filtering for single-spatial-mode operation of large-mode-area fiber amplifiers," *IEEE J. of Sel. Topics in Quantum Electron.* 15, 30-36 (2009).

- 
7. H. Rao, M. J. Steel, R. Scarmozzino, and R. M. Osgood, Jr., "Complex propagators for evanescent waves in bidirectional beam propagation method," *J. Lightwave Technol.* 18(8), 1155–1160 (2000).
  8. J. R. Marciante, V. V. Shkunov, and D. A. Rockwell, "Semi-guiding high-aspect-ratio core (SHARC) fiber amplifiers with ultra-large core area for single-mode kW operation in a compact coilable package," *Opt. Express*, vol. 20, 20238–20254 (2012).
  9. H. W. Bruesselbach, D. S. Sumida, R. A. Reeder, and R. W. Byren, "Low-heat high-power scaling using InGaAs diode-pumped Yb:YAG lasers," *IEEE J. Sel. Top. Quantum Electron.* 3(1), 105–116 (1997).
  10. J. R. Marciante and J. D. Zuegel, "High-gain, polarization-preserving, Yb-doped fiber amplifier for low-duty-cycle pulse amplification," *Appl. Opt.* 45(26), 6798–6804 (2006).
  11. Y. Chung and N. Dagli, "An assessment of finite difference beam propagation method," *IEEE J. Quantum Electron.* 26(8), 1335–1339 (1990).
  12. J. Yamauchi, T. Ando, and H. Nakano, "Beam propagation analysis of optical fibres by alternating direction implicit method," *Electron. Lett.* 27(18), 1663–1666 (1991).
  13. G. R. Hadley, "Transparent boundary condition for the beam propagation method," *IEEE J. Quantum Electron.* 28(1), 363–370 (1992).
  14. C. Jauregui, T. Eidam, H.-J. Otto, F. Stutzki, F. Jansen, J. Limpert, and A. Tünnermann, "Physical origin of mode instabilities in high-power fiber laser systems," *Opt. Express* 20, 12912–12925 (2012).
  15. S. Naderi, I. Dajani, T. Madden, and C. Robin, "Investigations of modal instabilities in fiber amplifiers through detailed numerical simulations," *Opt. Express* 21, 16111–16129 (2013).
  16. D. C. Brown and H. J. Hoffman, "Thermal, stress, and thermo-optic effects in higher average power double-clad silica fiber lasers," in *IEEE J. of Quant. Electron.* 37, 207–217 (2001).
  17. T. Eidam, C. Wirth, C. Jauregui, F. Stutzki, F. Jansen, H.-J. Otto, O. Schmidt, T. Schreiber, J. Limpert, and A. Tünnermann, "Experimental observations of the threshold-like onset of mode instabilities in high power fiber amplifiers," *Opt. Express* 19, 13218–13224 (2011).
  18. C. Robin, I. Dajani, C. Zeringue, B. Ward, and A. Lanari, "Gain-tailored SBS suppressing photonic crystal fibers for high power applications," *Proc. SPIE 8237, Fiber Lasers IX: Technology, Systems, and Applications*, 82371D (2012).
  19. K. R. Hansen, T. T. Alkeskjold, J. Broeng, and J. Lægsgaard, "Thermally induced mode coupling in rare-earth doped fiber amplifiers," *Opt. Lett.* 37, 2382–2384 (2012).
  20. F. Jansen, F. Stutzki, H.-J. Otto, T. Eidam, A. Liem, C. Jauregui, J. Limpert, and A. Tünnermann, "Thermally induced waveguide changes in active fibers," *Opt. Express* 20, 3997–4008 (2012).
  21. J. R. Marciante, V. V. Shkunov, and D. A. Rockwell, "Thresholds for thermal lensing and mode compression in high-power large-mode-area fiber amplifiers," manuscript in preparation for *Opt. Express*.
  22. Z. S. Eznaveh, G. Lopez-Galmiche, E. Antonio-Lopez, and R. Amezcua-Correa, "Bi-directional pump configuration for increasing thermal modal instabilities threshold in high power fiber amplifier," *Proc. of SPIE Vol. 9344, 93442G-1-93442G-5* (2015).

- 
23. C. Jauregui, H.-J. Otto, J. Limpert, and A. Tünnermann, "Mode instabilities in high-power bidirectional fiber amplifiers and lasers," in *Advanced Solid State Lasers*, OSA Technical Digest (online) (Optical Society of America, 2015), paper ATh2A.24.
  24. W. Guan and J. R. Marciante, "Pump-induced, dual-frequency switching in a short-cavity, ytterbium-doped fiber laser," *Opt. Express*, vol. 15, 14979-14992 (2007).
  25. J. R. Marciante, R. G. Roides, V. V. Shkunov, and D. A. Rockwell, "Near-diffraction-limited operation of step-index large-mode-area fiber lasers via gain filtering," *Opt. Lett.* 35(11), 1828–1830 (2010).
  26. T. Eidam, S. Hädrich, F. Jansen, F. Stutzki, J. Rothhardt, H. Carstens, C. Jauregui, J. Limpert, and A. Tünnermann, "Preferential gain photonic-crystal fiber for mode stabilization at high average powers," *Opt. Express* 19(9), 8656–8661 (2011).



## DISTRIBUTION LIST

DTIC/OCP 8725 John J. Kingman Rd, Suite 0944 Ft Belvoir, VA 22060-6218	1 cy
AFRL/RVIL Kirtland AFB, NM 87117-5776	1 cy
Nader Naderi Official Record Copy AFRL/RDLT	1 cy